



Universiteit  
Leiden  
The Netherlands

## **Deciphering the complex paramagnetic NMR spectra of small laccase**

Dasgupta, R.

### **Citation**

Dasgupta, R. (2021, June 15). *Deciphering the complex paramagnetic NMR spectra of small laccase*. Retrieved from <https://hdl.handle.net/1887/3188356>

Version: Publisher's Version

License: [Licence agreement concerning inclusion of doctoral thesis in the Institutional Repository of the University of Leiden](#)

Downloaded from: <https://hdl.handle.net/1887/3188356>

**Note:** To cite this publication please use the final published version (if applicable).

Cover Page



Universiteit Leiden



The handle <https://hdl.handle.net/1887/3188356> holds various files of this Leiden University dissertation.

**Author:** Dasgputa, R.

**Title:** Deciphering the complex paramagnetic NMR spectra of small laccase

**Issue Date:** 2021-06-15

# Chapter 1

---

## Introduction

---

*The Road goes ever on and on,  
Down from the door where it began.  
Now far ahead the Road has gone,  
And I must follow, if I can,*

*Pursuing it with eager feet,  
Until it joins some larger way  
Where many paths and errands meet.  
And whither then? I cannot say.*

*– John Ronald Reuel Tolkien*

## 1.1 General introduction

Enzymatic biofuel cells (EBCs) promise a sustainable and energy efficient future. It is a type of fuel cell that uses enzymes to catalyse redox reactions rather than precious non-renewable metals (platinum, palladium, ruthenium, etc.). A typical EBC oxidizes substrates at the anodic half, while reducing oxygen to water at the cathodic half. The anode can be functionalized with different enzymes depending on the application, for example using glucose dehydrogenase to oxidize glucose and act as biosensors for insulin delivery.(1) The cathode is usually functionalized with a multicopper oxidase (MCO), such as laccase, for the oxygen reduction reaction, due to their high efficiency and low required overpotential.(2, 3) The efficiency of a fuel cell is reflected by the power density of the system that represents the electron production rate.(2, 4) The traditional fuel cells can afford power densities in the order of a few kilowatts while the EBCs can generate power densities in the range of microwatts to milliwatts.(4) This limits the application of the EBCs to small devices, for example pacemakers (5), biosensors (6), wristwatches (7, 8), light-emitting diodes (9–11), music play back devices (12) and generating electricity from sunlight (13). Although there has been major advances in the application of EBCs, their commercial application remains elusive.(2, 14) It was estimated that an enzyme with a  $100 \text{ nm}^2$  cross section and an activity of 500 electrons per second can generate a current density of  $80 \mu\text{A}\cdot\text{cm}^{-2}$ .(15) For practical applications a biofuel cell will require a current density of  $10 \text{ mA}\cdot\text{cm}^{-2}$  that will necessitate loading of thousands of monolayers of enzyme on the electrodes.(4, 15) This poses a considerable engineering problem in addition to the challenges of improving the electron transfer from the enzyme to the electrodes and the life time of the enzyme.

One of the major contributors in defining the efficiency of a fuel cell is the oxygen reduction reaction at the cathodic half.(16) This reaction is a 4-electron reduction of molecular oxygen to water that has a reduction potential of 1.23 V. The major challenges in the oxygen reduction reaction that hinder the wide spread application of the fuel cells are the slow kinetics and the high required overpotential, which limits the thermodynamic efficiency to  $\sim 40\text{-}60\%$ .(17) The origin of the overpotential is the strong dioxygen bond with a bond energy of 498 kJ/mol.(18) In a traditional fuel cell platinum or its alloy is used as the cathode catalyst, providing an overpotential of  $\sim 300 \text{ mV}$ . However, its high cost renders industrial applications impractical.(17) In contrast, the EBCs uses laccase to perform the oxygen reduction reaction, with a very low overpotential of  $\sim 20 \text{ mV}$ , and a turn-over rate of 2.1  $\text{O}_2$  per laccase per second.(19) Although functionalizing laccase on the electrode seems promising, its limitations outweighs its effectiveness. The commonly encountered limitations are the enzyme instability, inhibition by high salt concentrations ( $\geq 100$

## Introduction

mM), low pH range of activity, large scale production of the enzyme and difficulty in achieving high packing densities due to the large size of laccase.(2, 17, 20) One way to overcome such limitations is to design an artificial “bio-inspired” catalyst.(20, 21) Extensive research is being carried out to synthesize efficient artificial catalysts for the oxygen reduction reaction based on the active site of laccase and in recent years several candidates were reported (Table 1.1, for a detailed list of copper based catalysts for oxygen reduction reaction (ORR), refer to Thorseth *et al.*(17)).(20) It is evident that most of the artificial catalysts are either mononuclear or binuclear copper complexes and the most efficient catalyst was reported to be Cu-Hdatrz (Table 1.1). However, the power density generated falls below the platinum based catalyst.(17) Ligand modification such as using pyridine, pyrrole, imidazole and triazole in association with bridging moieties between the copper centres were shown to improve the overall performance of the catalyst but the enzyme laccase remains the most efficient in terms of overpotential and turnover frequency per active site.(17, 20, 22) Improvement of the turnover frequency per site was reported for polymeric copper based catalysts, such as Cu(3, 3'-diaminobenzidine) (21), and self-assembled monolayer based systems (20), due to their high stability but minimal improvement was observed in terms of overpotential.(21)

There are multiple factors affecting the efficiency of such “bio-inspired” catalysts. First, the geometry of the primary coordination sphere that can stabilize different binding modes of dioxygen results in different reaction mechanisms, i.e.  $4e^-/4H^+$  conversion of dioxygen to water or  $2e^-/2H^+$  conversion of dioxygen to hydrogen peroxide.(22–24) The coordination of the active site in laccase (described in section 1.2) was shown to be in an “entatic state” with a distorted tetrahedral geometry, thereby attaining a conformation that compromises between the favoured geometries for Cu(I) and Cu(II) ions.(25–28) Such a state reduces the reorganization energy of the reaction and enables the protein to transfer electrons efficiently.(26, 27) In laccase, the type 1 copper site (described in section 1.2) was studied extensively, showing that the reorganization energy was  $\sim 0.5$  eV upon reduction of the copper ion by extracting an electron from substrate. In contrast, the reorganization energy of the substrate was in the range of 1.2 to 2.0 eV. This suggests that the geometry of the T1 site in the protein does not change much and is in an entatic state, while the geometry of the substrate does change.(25, 29) Creating an entatic state of the metal coordination in artificial catalysts poses a challenge for synthesis. A few successful attempts have been reported for a heme based oxygen activation system, and recently for copper based photoactive complexes, aiming for efficient electron transfer.(27, 30)

Second, it was shown that in the laccase second coordination sphere residues like aspartic acid or glutamic acid are important in regulating the proton chemical potential and stabilizing the intermediate states.(31–33) This idea was implemented in an iron-porphyrin based system with a carboxyphenyl group in the second

# Introduction

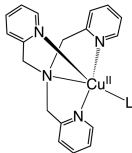
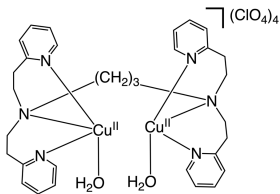
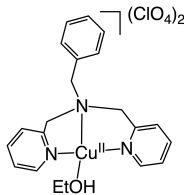
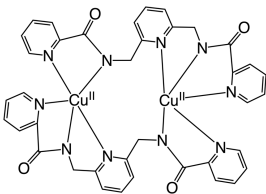
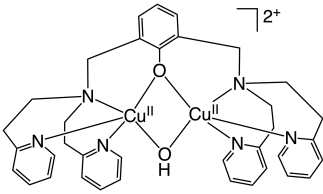
coordination sphere where the carboxylic groups are oriented toward the redox centre, acting as a proton relay.(34) However, the overpotential was observed to be  $\sim 400$  mV, 20 times higher than that of laccase.

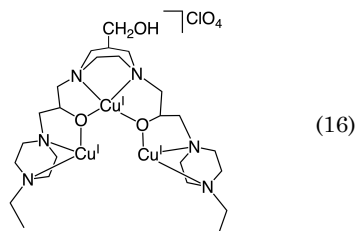
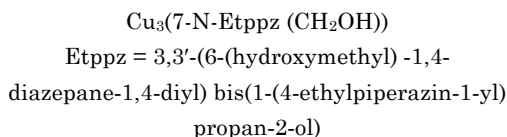
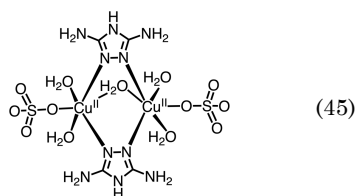
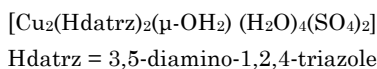
This leads to the final factor that can affect the efficiency of these catalysts, the motions at the redox active site. Oxygen reduction catalysed by laccase is a complicated reaction comprising a series of steps, including several electron transfer steps, oxygen binding, bond breaking, proton transfers through the enzyme, protonation and water release (the detailed reaction mechanism in laccase is shown in section 1.2).(25, 29). The function of the enzyme is two-fold, lowering the activation barriers of each of the consecutive steps and ensuring that all steps occur in the desired order, avoiding side products. Enzymes speed up reactions by stabilizing transition states with favourable interactions in the active site. Lowering proton transfer barriers may require an enzyme conformation different from the one required to lower the barrier for oxygen-oxygen bond breaking. Thus, it seems almost inevitable that laccase uses different conformations during the catalytic cycle, implying motions must occur. Such a sophisticated approach of catalysis requires a system with many atoms and it may well be fundamentally impossible to mimic that with low molecular weight compounds (Table 1.1) in detail. Examples of such motions is ubiquitous in enzymes. For example in alcohol dehydrogenase the binding of substrate  $\text{NAD}^+$  causes conformational changes in the active site that reduces the barrier for proton transfer.(35) Similarly, the substrate free adenylate kinase was found to undergo preferred motions in  $\mu\text{s}$ -ms time scale to attain substates along the reaction coordinate.(36)

Extensive studies on the dynamics at the TNC of laccase have not been reported but observations from crystal structures (PDB entries 2xu9 (37) and 3zx1 (38)) show that active site histidine imidazole rings can attain two conformations without breaking the coordination with the coppers. Investigating the dynamics of the TNC at the atomic level is non-trivial. A crystal structure shows a time-averaged conformation. Nuclear magnetic resonance (NMR) spectroscopy in solution suffers from the large size of the enzyme, and line broadening caused by the paramagnetic copper ions. The research described in this thesis is based on paramagnetic NMR spectroscopy to probe motions or conformational heterogeneity at the TNC of a laccase. A two-domain small laccase from *Streptomyces coelicolor* (SLAC) (39) is employed, because of its thermostability, ease of large-scale production, resistance to high salt concentrations ( $\sim 1$  M) and  $\text{pH} \geq 7.0$ .(39–41) Although using SLAC directly on an electrode looks promising, the low turnover frequency and limited stability hinders upscaling for application.(42) This study can help in designing a functional framework for efficient “bio-inspired” oxygen reduction catalysts that can be applied for longer term usage. Maybe, a small low molecular weight protein or peptide mimic of the active site of laccase can be advantageous.

# Introduction

**Table 1.1.** Examples of oxygen reduction catalysts based on the active site of laccase.

| Catalyst  | Structure   | Ref. |
|---|---|------|
| $[\text{Cu}(\text{tmpa})(\text{L})]^{2+}$<br>tmpa = tris(2-pyridylmethyl) amine<br>L = (trifluoromethanesulfonate) <sub>2</sub>   |    | (43) |
| $[\text{Cu}^{\text{II}}_2(\text{N}3)(\text{H}_2\text{O})_2](\text{ClO}_4)_4$<br>N3 = (– (CH <sub>2</sub> ) <sub>3</sub> –linked (bis[2-(2-pyridyl) ethyl] amine) <sub>2</sub> ) |    | (23) |
| $[\text{Cu}^{\text{II}}(\text{BzPY}1)(\text{EtOH})](\text{ClO}_4)_2$<br>BzPY1 = N-Benzyl-N, N-bis(2-pyridinylmethyl) amine  |    | (23) |
| Copper complex with polypyridine-polyamide ligand   |  | (44) |
| $[\text{Cu}^{\text{II}}_2(\text{LO})\cdot(\text{OH})]^{2+}$<br>[LO = bi-nucleating ligand with copper-bridging phenolate moiety]  |  | (24) |



## 1.2 The multicopper oxidase: Laccase

Laccase is a multi-copper oxidase (MCO) comprising two active sites, a type 1 (T1) site for oxidizing substrates and a tri-nuclear copper centre (TNC) for the oxygen reduction reaction (Figure 1.1). The type 1 site is also known as the blue copper site and consists of a copper ion coordinated to a cysteine sulphur, and two histidine ligands. An additional axial methionine can coordinate the copper in case of the low (100 to 400 mV) redox potential laccases (Figure 1.2a and c). The TNC is comprised of a type 3 (T3) and a type 2 (T2) copper site. A T3 site is characterized by a binuclear copper centre in which each copper ion is coordinated by three histidine ligands and the copper ions are bridged by a hydroxide. A T2 site is characterized by a copper centre coordinated by two histidine ligands and a water derived ligand (water or hydroxide ion). The T1 and T2 sites are electron paramagnetic resonance (EPR) active, while the T3 site is EPR silent due to the strong antiferromagnetic coupling between the electron spins on the cupric ions.(25)

Laccases can be divided into two classes, three-domain monomeric laccases and two-domain trimeric small laccases (Figure 1.1). Three-domain laccases are further divided into low redox potential (100 to 400 mV) and high redox potential (> 400 mV) laccases, based on the redox potential of the T1 site. Three-domain laccases are widely distributed among different domains of life, while the two-domain small laccases are found mostly in prokaryotes.(46) The T1 copper ions of the two-domain small laccases and the low redox potential three-domain laccases are coordinated by an additional axial methionine, which was shown to be the reason for their low redox potential.(47–49) For the three-domain laccases lacking this axial methionine ligand



# Introduction

and in combination with a hydrophobic environment of the T1 site, the high redox potential is high (Figure 1.2).(40, 48, 50) Both the two-domain small laccases and three-domain laccases were subjected to many directed evolution and site-directed mutation studies to raise the redox potential of the T1 site and to increase the high pH stability.(48, 50–52) In recent years, the T1 site of the two-domain small laccase was successfully modified to have a redox potential comparable to the high redox potential fungal laccases.(48, 50, 53) Table 1.2 shows the redox potential of different small laccases (for the detailed list of the redox potentials of different laccases refer to Mate *et al.* (49)). It is observed that replacing the methionine residues with more hydrophobic residues near the T1 site increases the redox potential drastically.(50) In addition to improving the T1 site redox potential, studies were performed to improve the activity of small laccase by site directed mutagenesis.(40, 54, 55) Table 1.3 summarizes the mutants that showed higher activity than the wild type. Two such mutants have been reported, H165A, located near the T3 site, and Y230A, near the T1 site (Figure 1.2). The increase in activity was attributed to enhanced accessibility of the copper ions and oxygen in the T3 site and improvement in substrate binding, respectively.(40, 55)

**Table 1.2.** Redox potentials of the T1 sites of native small laccases and variants.

| Laccase                         | Source                      | Redox potential<br>(T1 site) | Reference |
|---------------------------------|-----------------------------|------------------------------|-----------|
| SvSL                            | <i>S. viridochromogenes</i> | 350 ± 7 mV                   | (56)      |
| Ssl1                            | <i>S. sviveus</i>           | 375 ± 8 mV                   | (50)      |
| SLAC                            | <i>S. coelicolor</i>        | 430 mV                       | (42)      |
| Ssl1<br>M295L/M293G/M195A/V287N | <i>S. sviveus</i>           | 560 ± 6 mV                   | (53)      |

**Table 1.3.** Small laccase mutants that showed higher substrate oxidation activity than wild type.

| Laccase | Source                 | Mutant | Activity (mutant/wild type)<br>(nM min <sup>-1</sup> µg <sup>-1</sup> ) | Reference |
|---------|------------------------|--------|---|-----------|
| SLAC    | <i>S. coelicolor</i>   | Y230A  | 1.20/0.98   | (40)      |
| SgtfSL  | <i>S. griseoflavus</i> | H165A  | 1.45/0.82   | (55)      |

Also, the TNCs differ between the two-domain and three-domain laccases. In the former three TNCs are located at the interfaces of the three subunits, while in the

## Introduction

three-domain laccases, a single TNC is found at the interface of two domains (Figure 1.1). In the small laccases the coppers in the TNC are coordinated by His N $\epsilon$ 2 atoms, whereas in three-domain laccases one of the T3 coppers has a N $\delta$ 1 as a coordinating atom. Residues in the second coordination sphere of the TNC are also different between small laccases and three-domain laccases. In the former, the second coordination sphere is mostly occupied by polar residues, except for I169 and A266. It has been hypothesized that due to this polarity near the TNC of the two-domain SLAC it has greater tolerance for high pH and high salt concentration.(54, 55) In three-domain laccases most second shell residues are hydrophobic, except for the glutamates and aspartates near the T3 and the T2 sites (Figure 1.2). In three-domain laccases the aspartic/glutamic acid in the second coordination sphere of the T3 site was shown to be a proton donor, while the aspartate near the T2 site is an acceptor, keeping the total charge of the TNC constant during the proton transfer process of the oxygen reduction reaction (Figure 1.2e and f).(31, 32, 57) Similar arrangements of polar residues at the entrances of the water channel can be observed in the crystal structures of small laccases. Here, protons can be donated by the glutamine or serine near the T3 site and accepted by the aspartate near the T2 site. However, there is no experimental or theoretical proof for such a process in small laccase. A common feature of the two-domain and three-domain laccases is the presence of a water channel that passes through the TNC (Figure 1.2d, e and f), providing the entry path for protons required for the formation of water. It was reported that the tyrosine near the T2 site is a unique feature of small laccase, as it allows free radical formation during the oxygen reduction reaction.(58–60) Recently, a study using side directed mutagenesis showed that His164 (Figure 1.2d; numbering from PDB 3cg8) acts a gatekeeper residue for dioxygen entry.(55) Mutating it to alanine increased the activity of the small laccase (Table 1.2).(55) Similar gatekeeper residue was not yet reported for the three-domain laccase. The structural, biochemical and sequence analysis of the two-domain small laccase and three-domain laccase suggests that they originated from a common ancestor and later differentiated to serve the same function in different conditions.(46)

# Introduction

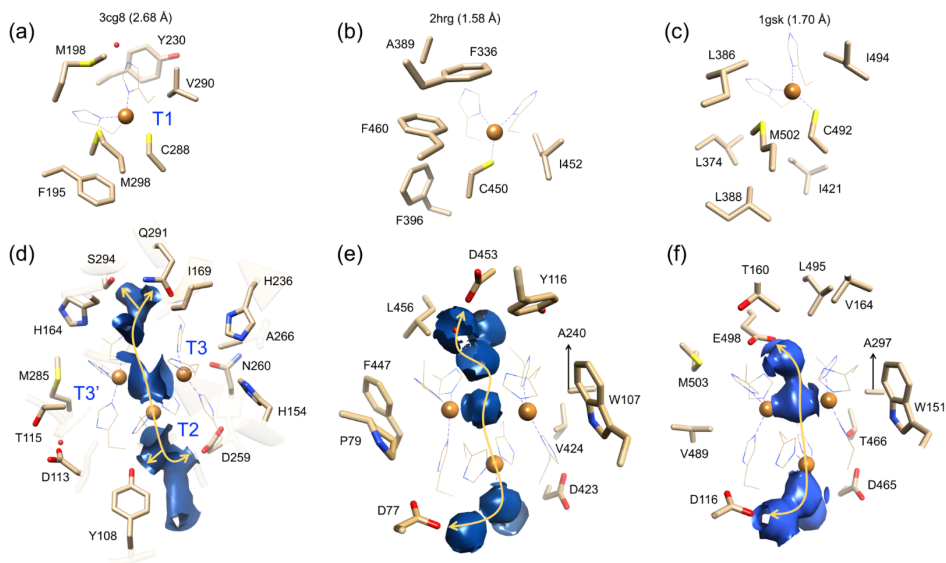
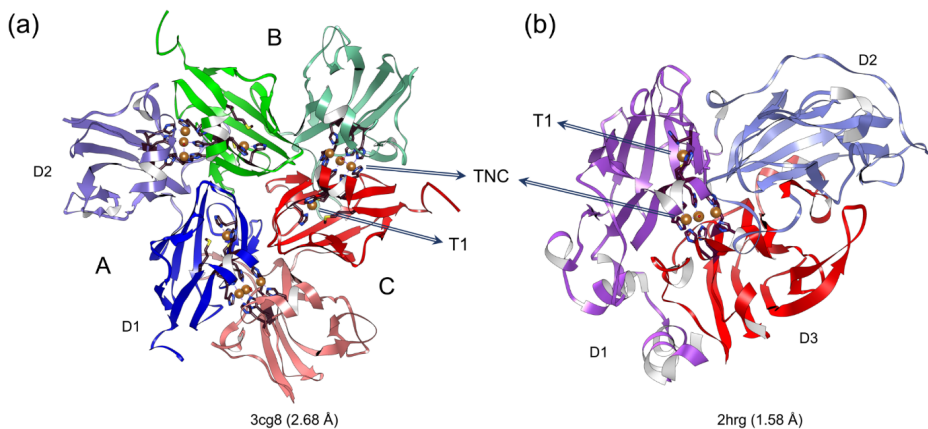


**Figure 1.2.** (a-c) T1 sites of small laccase from *S. coelicolor* (a),(61) the high redox potential three-domain laccase from *T. troglodytes* (b),(62) and the low redox potential three-domain laccase from an endospore coat of *Bacillus subtilis* (c).(63) (d-f) The water channels shown as the electron density surface of the water molecules in the TNC in the crystal structures of the laccases in panels (a-c). The double-sided arrows show possible proton transfer paths. Coordinating histidine ligands are shown as wire and second coordination sphere residues are shown as sticks. Red spheres are the bound water molecules. The copper sites are marked in panels a and d.

---

The oxygen reduction reaction is summarized in Figure 1.3 and 1.4b.(29, 32, 58, 60, 64, 65) The resting oxidized (RO) state is reduced to the fully reduced (FR) state by four electrons that are provided by oxidation of substrates at the T1 site (Figure 1.2, 1.3 and 1.4b). The FR state binds oxygen and reduces it to a peroxide intermediate (PI) state by two-electron transfer (Figure 1.4b). The subsequent conversion of the PI to the native intermediate (NI) state requires two more electrons. The third cuprous copper ion supplies one electron and the second can be obtained from either the tyrosine near the T2 site in small laccase or the T1 site (Figure 1.3 and 1.4b). In the small laccase from *S. coelicolor* (SLAC), the Y108 residue (Figure 1.2a) was reported to provide this electron to the T2 copper, when the T3 site copper ions are reduced (Figure 1.3).(58, 60) A similar observation was made for human ceruloplasmin, in which the tyrosine radical is formed during the conversion of RO state to the FR state.(58, 66) Without substrate the NI state is slowly converted to the RO state, while it is rapidly converted to the FR state with excess of substrates present.(65) The basic structure for the catalytic motif of the TNC in the RO state is shown in Figure 1.4a.(32, 65, 67) This structure is shared among all the laccases and is used for density functional theory (DFT) calculations. It is particularly suited for modelling entatic states since the overall charge and spin state of the catalytic motif can be defined without resolving spin and charge down to the level of individual magnetic ions and histidine side chains. This provides room for structural flexibility such as histidine ring motions at the active site. The modelling of the catalytic motif can also be aided by defining the redox couples during the oxygen reduction reaction (Figure 1.4b) where the charge and spin multiplicities are stated. For small laccases and human ceruloplasmin the tyrosine near the T2 site is also involved in the catalytic mechanism as mentioned above (Figure 1.3). The present model of the oxygen reduction reaction at the TNC however, does not consider the motions that can help in attaining a conformation that can reduce the energy barrier for electron and proton transfer.

# Introduction

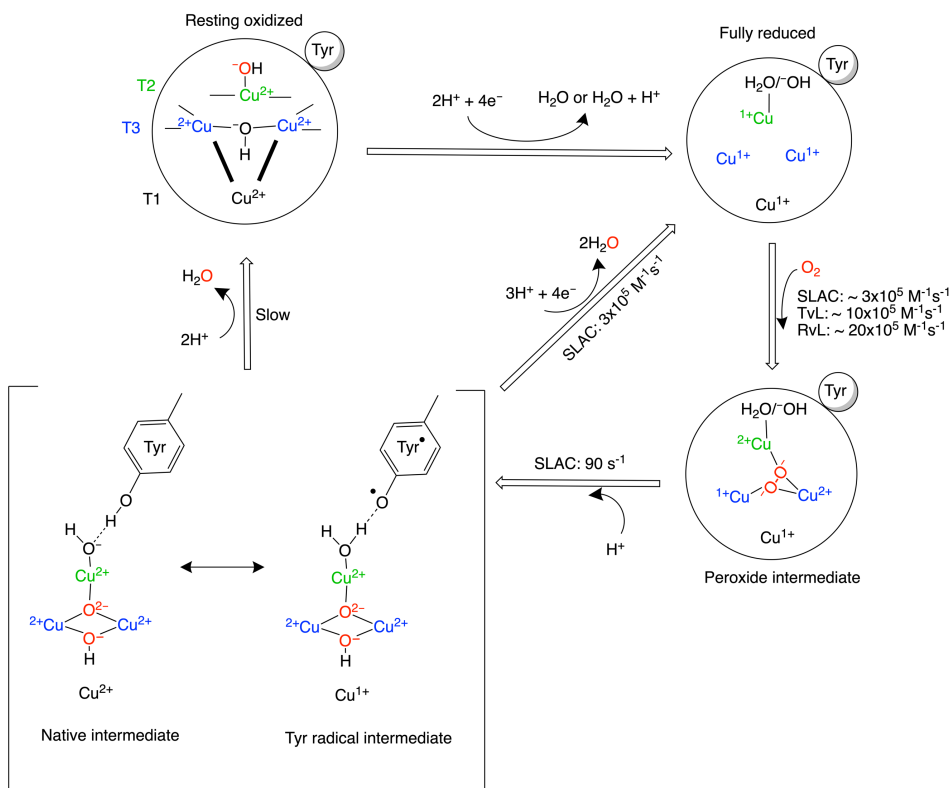


**Figure 1.3:** Reaction mechanism of the oxygen reduction reaction in SLAC. The coordination of the coppers in the TNC is shown in the resting oxidized state with the T3 coppers (blue) coordinated by three His Nε2 atoms each and the hydroxyl group, whereas the T2 copper (green) is coordinated by two His Nε2 atoms and a hydroxide/water.(32, 57, 65) The oxygen binding rates are shown for laccases from several organisms, SLAC from *S. coelicolor*, TvL from *Trametes versicolor* laccase and RvL for *Rhus vernicifera* laccase.(65) A tyrosine radical intermediate for SLAC is shown.(58) The formation of the tyrosine radical intermediate was reported only for small laccase and human ceruloplasmin.(66) The O atom is coloured red to show that it is from the oxygen molecule undergoing reduction. Only the stable intermediate states are denoted for the transition states in-between readers are referred to Solomon et al. (64, 65)

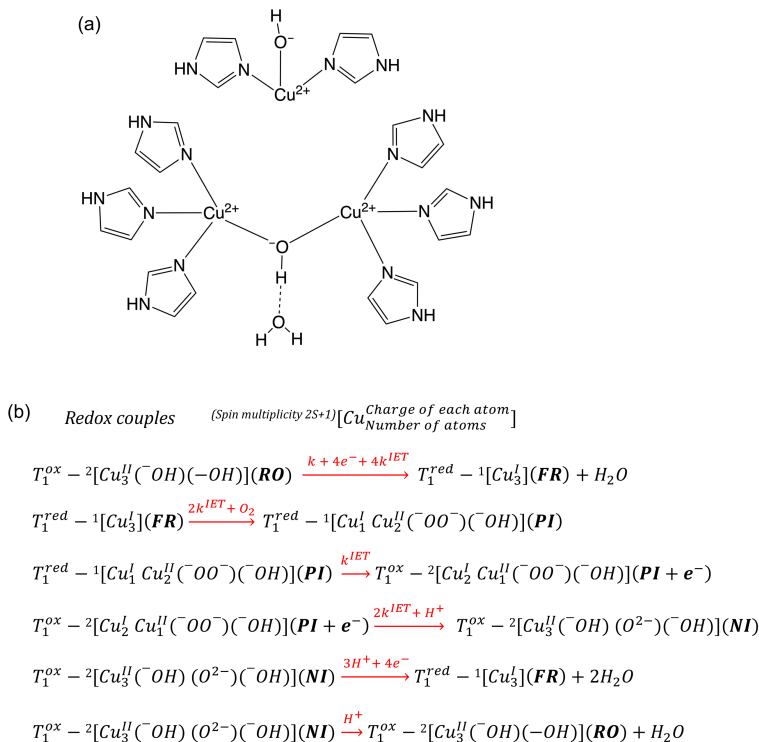


**Figure 1.4:** (a) The starting minimal model of the TNC in the RO state used by Solomon *et al.*, to describe the reaction mechanism using DFT calculations. (32, 65, 67) The coordinating histidine ligands are replaced with the imidazolyl groups. The charges of the copper ions and the hydroxide ions are shown. (b) The redox couples describing the reaction mechanism of the oxygen reduction by the TNC. The spin multiplicities associated with each catalytic state, the charges of the copper ions and oxygen atoms are shown. In the reaction  $k$  represents the rate of substrate oxidation at the T1 copper site and  $k^{\text{IET}}$  represents the intramolecular electron transfer rate.

## 1.3 Paramagnetic nuclear magnetic resonance spectroscopy

Studying the TNC with NMR spectroscopy is complicated by several factors. SLAC is a protein of more than 100 kDa in the native trimeric form, making the application of standard techniques for backbone assignment of resonances very challenging. However, the signals of nuclear spins around the coppers in oxidized form have properties that vary greatly from those of nuclear spins far away. The latter will have relatively short transverse and very long longitudinal relaxation times due to the

# Introduction

slow tumbling of the protein in solution, resulting in broad lines and long repetition times. For the nuclei interacting with the strong electron spins, which are on the cupric ions and delocalized over the ligands, the signals experience large chemical shift changes and strongly reduced relaxation times for both transverse and longitudinal relaxation. These features make it possible to selectively detect the signals of nuclear spins near the paramagnetic centres by rapid repetition of NMR scans, combined with long measurement times for sufficient signal-to-noise data and analysis of the spectral region outside the normal envelope of signals for non-paramagnetically shifted peaks. Paramagnetically tailored experiments are necessary to compensate for the short transverse relaxation times, which lead to rapid loss of coherence during the pulse sequence.(68) The observed chemical shift ( $\delta_{\text{obs}}$ ) is given by (68)

$$\delta_{\text{obs}} = \delta_{\text{dia}} + \delta_{\text{FCS}} + \delta_{\text{PCS}} \quad (1.1)$$

where  $\delta_{\text{dia}}$  is the diamagnetic chemical shift,  $\delta_{\text{FCS}}$  the Fermi contact shift (FCS) and  $\delta_{\text{PCS}}$  the pseudo-contact shift (PCS).

## Fermi contact shift

The FCS is due to the additional magnetic field generated at the nucleus due to the time-averaged electron spin density that is delocalized from the nearby paramagnetic metal. It is a through bond interaction and is generally observed for nuclei that are  $\leq 5$  bonds away from the metal centre.(68) For a single metal centre, the  $\delta_{\text{FCS}}$  is given by

$$\delta_{\text{FCS}} = \frac{A g_e \mu_B S(S+1)}{\hbar 3\gamma k_B T} \quad (1.2)$$

where  $A$  is the isotropic hyperfine coupling constant,  $g_e$  is the free-spin electron  $g$  factor with the value of 2.0023,  $\mu_B$  is the electron Bohr magneton,  $\hbar$  is the reduced Planck constant,  $\gamma$  is the gyromagnetic ratio of the nucleus,  $k_B$  is the Boltzmann constant,  $T$  is the temperature in Kelvin and  $S = 1/2$ , which is in this case the electron spin of the Cu(II) ion.  $A$  is directly proportional to the spin density  $\rho$  on the nucleus and is given by (68)

$$A = \frac{2}{3} \hbar \gamma_I \mu_B g_e \mu_0 \rho \quad (1.3)$$

The sign of the FCS is determined by the polarization of the electron spin. If the spin is parallel to the external magnetic field, the sign is positive and if it is anti-parallel to the external magnetic field, the sign is negative.

In the case of coupled multiple metal centers, as is the case for the TNC of laccase, the FCS is given by (68)

$$\delta_{\text{FCS}} = A \frac{\mu_B g_e}{\hbar \gamma_I 3k_B T} \frac{\sum_{C_i S_T} C_i S_T (S_T + 1) (2S_T + 1) e^{-E(S_T)/k_B T}}{\sum_{S_T} (2S_T + 1) e^{-E(S_T)/k_B T}} \quad (1.4)$$

# Introduction

where  $S_T$  is the total electronic spin calculated by Kambe's approach.(69–71)  $C_i$  is the ratio of the spin expectation value for the metal ion in Fermi contact with the respective nucleus and the total spin expectation value of all the coupled metal ions.(39, 68)  $E_{(S_T)}$  are the eigen values for all the states of  $S_T$ .

For a two-spin antiferromagnetically coupled system such as the T3 coppers in the RO state of the TNC equation 1.4 is expressed as (68)

$$\delta_{\text{FCS}} = \frac{A g_e \mu_B}{\hbar \gamma k_B T} \left[ \frac{e^{\left(\frac{2J}{k_B T}\right)}}{1 + 3e^{\left(\frac{2J}{k_B T}\right)}} \right] \quad (1.5)$$

where  $2J$  is the energy different between the singlet ( $S_T = 0$ ) ground state and the excited triplet state ( $S_T = 1$ ).

For a three-spin coupled system like the NI state of the TNC, the derivation is more complicated. Following Kambe's approach (69–71), the total spin  $S_T$  of a three spin1/2 system can take values of 1/2, 1/2 and 3/2. The two coupled metal centers with spin 1/2 each, form a subunit that can have a spin 1 or 0 ( $S_i + S_j \dots S_i - S_j$ ). These states can interact with the third copper ion with spin 1/2. For the two-spin state 0 coupled to the third spin 1/2 a ground state  $\left|\frac{1}{2}, 0\right\rangle$  can be identified, and for the two-spin state 1 coupled to the third spin 1/2 a first excited doublet state  $\left|\frac{1}{2}, 1\right\rangle$  and a second excited quartet state  $\left|\frac{3}{2}, 1\right\rangle$  are possible due to the higher spin multiplicity for this arrangement.(64, 72).

The expression for  $C_i$  depends on the relative strengths of the electronic  $J$  couplings between the metal centers in the TNC and is summarized in Table 1.4.(73) The energy levels can be calculated from the Heisenberg Hamiltonian for  $n$  interacting spins, (71)

$$\hat{H} = -2 \sum_{j>i=1}^n J_{ij} S_i \cdot S_j \quad (1.6)$$

where  $J_{ij}$  is the exchange coupling between  $S_i$  and  $S_j$  spins and  $n=3$ . There will be in total 8 microstates ( $M_{xyz}$ , where xyz are the spin state of each spin) for a three coupled system. Operating the Hamiltonian in equation 1.6 on each microstate  $\langle M_{xyz} | \hat{H} | M_{xyz} \rangle$ , we get an 8x8 matrix (M1) for the interaction. Solving for the eigenvalues, we get the expression for  $E_{(S_T)}$  for each of the energy states (ground state, the first excited doublet state and the second excited doublet state). The expression for  $E_{(S_T)}$  in different symmetric conditions of the  $J$  coupling ( $J_{13}$ ,  $J_{12}$ ,  $J_{23}$ ) between the copper pairs is summarized in (Table 1.5).(64, 71, 74)



## Introduction

**Table 1.4.** Expression for  $C_i$  in equation 1.4 for a three spin 1/2 coupled system as in the native intermediate state of the TNC (Figure 1.3). (a)  $J_{13} = J_{12} = J_{23} = J$  or  $J_{13} = J_{12} = J \neq J_{23}$  and (b)  $J_{13} \neq J_{12} \neq J_{23}$

| States                              | (a)   |       |       | (b)   |  |  |
|-------------------------------------|-------|-------|-------|---|--|--|
|                                     | $C_1$ | $C_2$ | $C_3$ | $C_1$   | $C_2$  | $C_3$                                    |
| $\left \frac{3}{2}, 1\right\rangle$ | 1/3   | 1/3   | 1/3   | 1/3   | 1/3  | 1/3                                      |
| $\left \frac{1}{2}, 1\right\rangle$ | 2/3   | 2/3   | -1/3  | $\frac{2\alpha\sqrt{(1-\alpha^2)}}{\sqrt{3}}$<br>$+\frac{2-2\alpha^2}{3}$ | $-\frac{2\alpha\sqrt{(1-\alpha^2)}}{\sqrt{3}}$<br>$+\frac{2-2\alpha^2}{3}$ | $-\frac{1}{3}$<br>$+\frac{4\alpha^2}{3}$ |
| $\left \frac{1}{2}, 0\right\rangle$ | 0     | 0     | 1     | $-\frac{2\alpha\sqrt{(1-\alpha^2)}}{\sqrt{3}} + \frac{2\alpha^2}{3}$      | $\frac{2\alpha\sqrt{(1-\alpha^2)}}{\sqrt{3}} + \frac{2\alpha^2}{3}$        | $1 - \frac{4\alpha^2}{3}$                |

where,  $\alpha^2 = \frac{1}{2}(1 - \frac{1}{\sqrt{1+x^2}})$  and  $x = \sqrt{3}\frac{J_{12}-J_{13}}{2J_{23}-J_{12}-J_{13}}$ , assuming that  $J_{23}$  is the strongest coupling.(73)

**Table 1.5:** Eigenvalues for the states of  $S_T$  with (a)  $J_{13} = J_{12} = J_{23} = J$ , (b)  $J_{13} = J_{12} = J \neq J_{23}$  (c)  $J_{13} \neq J_{12} \neq J_{23}$ .

| Total spin $S_T$             | Eigenvalues $E_{(S_T)}$ |                             |  |
|------------------------------|-------------------------|-----------------------------|--|
|                              | (a)                     | (b)                         | (c)  |
| 3/2 $ \frac{3}{2}, 1\rangle$ | $-3\frac{J}{2}$         | $-\frac{1}{2}(2J + J_{23})$ | $-\frac{(J_{12} + J_{23} + J_{13})}{2}$    |
| 1/2 $ \frac{1}{2}, 1\rangle$ | $3\frac{J}{2}$          | $2J - J_{23}/2$             | $\frac{(J_{12} + J_{23} + J_{13})}{2} + X$ |
| 1/2 $ \frac{1}{2}, 0\rangle$ | $3\frac{J}{2}$          | $\frac{3(J_{23})}{2}$       | $\frac{(J_{12} + J_{23} + J_{13})}{2} - X$ |

$$X = \sqrt{J_{12}^2 + J_{13}^2 + J_{23}^2 - J_{12}J_{13} - J_{12}J_{23} - J_{13}J_{23}}$$

# Introduction

Matrix  $M1$  calculated by operating Hamiltonian in equation 1.6 on each microstate ( $M_{xyz}$ ) of a TNC with 3 coupled  $Cu^{2+}$  ions. ( $\uparrow = 1/2$  and  $\downarrow = -1/2$ )

| Microstates                      | $\uparrow\uparrow\uparrow$               | $\uparrow\uparrow\downarrow$             | $\uparrow\uparrow\downarrow$            | $\uparrow\uparrow\downarrow$            | $\uparrow\downarrow\downarrow$           | $\downarrow\uparrow\uparrow$            | $\downarrow\uparrow\uparrow$             | $\downarrow\uparrow\downarrow$ | $\downarrow\uparrow\downarrow$            | $\downarrow\downarrow\downarrow$ |
|----------------------------------|--|--|---|---|--|---|--|--------------------------------|---|----------------------------------|
| $\uparrow\uparrow\uparrow$       | $-\frac{1}{2}(J_{12} + J_{13} + J_{23})$ | 0  | 0                                       | 0                                       | 0  | 0                                       | 0  | 0                              | 0   | 0                                |
| $\uparrow\uparrow\downarrow$     | 0  | $\frac{1}{2}(-J_{12} + J_{13} + J_{23})$ | $-J_{23}$                               | $-J_{13}$                               | 0  | 0                                       | 0  | 0                              | 0   | 0                                |
| $\uparrow\downarrow\uparrow$     | 0  | $-J_{23}$                                | $\frac{1}{2}(J_{12} - J_{13} + J_{23})$ | $-J_{12}$                               | 0  | 0                                       | 0  | 0                              | 0   | 0                                |
| $\downarrow\uparrow\uparrow$     | 0  | $-J_{13}$                                | $-J_{12}$                               | $\frac{1}{2}(J_{12} + J_{13} - J_{23})$ | 0  | 0                                       | 0  | 0                              | 0   | 0                                |
| $\uparrow\downarrow\downarrow$   | 0  | 0  | 0                                       | $\frac{1}{2}(J_{12} + J_{13} - J_{23})$ | $-\frac{1}{2}(J_{12} + J_{13} - J_{23})$ | $-J_{12}$                               | $-J_{13}$                                | 0                              | 0   | 0                                |
| $\downarrow\uparrow\downarrow$   | 0  | 0  | 0                                       | 0                                       | $-\frac{1}{2}(J_{12} + J_{13} - J_{23})$ | $\frac{1}{2}(J_{12} - J_{13} + J_{23})$ | $-J_{23}$                                | $-J_{13}$                      | 0   | 0                                |
| $\downarrow\downarrow\uparrow$   | 0  | 0  | 0                                       | 0                                       | 0  | 0                                       | $\frac{1}{2}(-J_{12} + J_{13} + J_{23})$ | $-J_{23}$                      | $-\frac{1}{2}(-J_{12} + J_{13} + J_{23})$ | 0                                |
| $\downarrow\downarrow\downarrow$ | 0  | 0  | 0                                       | 0                                       | 0  | 0                                       | 0  | 0                              | $-\frac{1}{2}(J_{12} + J_{13} + J_{23})$  | 0                                |

# Introduction

The paramagnetic effect is temperature dependent, for two reasons. With increasing temperature, the populations of the low and high energy levels of an electron spin will become more similar, reducing the time-averaged effect on the nuclear spin, thereby decreasing the FCS (Curie behaviour). For coupled systems, increasing the temperature and thus  $k_B T$ , increases the population of the excited  $S = 1$  energy level, so enhancing the paramagnetic effect on the nuclear spin and thus, increasing the shift with temperature (anti-Curie behaviour).(68) Therefore, Curie behaviour is usually observed for signals of nuclear spins near a single copper site, while anti-Curie behaviour is observed for signals of spins near a coupled metal centre with a coupling strength of  $> 200 \text{ cm}^{-1}$ .(68)

## Pseudo-contact shift

The PCS is the contribution from the dipolar interaction of the time-averaged unpaired electron spin with the surrounding nuclear spins. It is due to the anisotropy of the magnetic susceptibility tensor ( $\chi$ ) of the metal ion that is observed *e.g.* when the metal ion has spin  $S \geq 1/2$  with a significant zero field splitting.(75) The metal ion contribution to the PSC (in ppm) is given by (76, 77)

$$\delta_{\text{PCS}} = \frac{1}{4\pi} \frac{10^6}{2r^3} \{ (1 - 3\cos^2\theta)(\chi_{zz} - \tilde{\chi}) + \sin^2\theta \cos 2\varphi (\chi_{yy} - \chi_{xx}) \} \quad (1.7)$$

where  $\chi_{xx}$ ,  $\chi_{yy}$  and  $\chi_{zz}$  are the principal axis components of the susceptibility tensor with isotropic  $\tilde{\chi} = \frac{1}{3}(\chi_{yy} + \chi_{xx} + \chi_{zz})$ ,  $\theta$  is the angle between the unit vector along the metal-ligand nuclei and the direction of the  $\chi_{zz}$  of the susceptibility tensor,  $r$  is the distance from the metal ion nucleus to the ligand nucleus and  $\varphi$  is the angle between the projection of unit vector along the line joining the metal and ligand nuclei in the  $xy$  plane and the  $x$  axis. If the electronic excited state is not thermally accessible at temperatures used for EPR and NMR studies, *i.e.* the ground state is far below any excited state, then the  $\chi$ -tensor is proportional to the  $g$ -tensor, which can be measured by EPR spectroscopy, according to (75, 76)

$$\chi_{ii} = \frac{\mu_0 \mu_B^2 S(S+1)}{3k_B T} g_{ii}^2, \quad (1.8)$$

where  $\mu_B$  is the Bohr magneton ( $9.2740 \times 10^{-24} \text{ J T}^{-1}$ ),  $S$  is the electronic spin with  $S = 1/2$  for a single  $\text{Cu}^{2+}$ ,  $k_B$  is the Boltzmann constant ( $1.3807 \times 10^{-23} \text{ J K}^{-1}$ ),  $\mu_0$  is the permeability of the vacuum ( $4\pi \times 10^{-7} \text{ kg m s}^{-2} \text{ A}^{-2}$ ) and  $T$  is the temperature in Kelvin. Substituting equation 1.8 in equation 1.7, the PCS is given by (76)

$$\delta_{\text{PCS}} = 10^6 \frac{\mu_0 \mu_B^2 S(S+1)}{4\pi 9k_B T r^3} \left\{ \left( g_{zz}^2 - \frac{1}{2} (g_{xx}^2 + g_{yy}^2) \right) (1 - 3\cos^2\theta) + \left( \frac{3}{2} (g_{yy}^2 - g_{xx}^2) \sin^2\theta \cos 2\varphi \right) \right\}. \quad (1.9)$$

For SLAC-T1D, it was reported that there is a low lying excited state which is  $\sim 125 \text{ cm}^{-1}$  (39) above the ground state and can be accessible at temperatures  $> 175 \text{ K}$ . Since

# Introduction

the NMR experiments were done at temperatures between 278 – 303 K, this excited state has to be taken into account to estimate the contribution of the PCS. For such a system the  $\chi$ -tensor from equation 1.8 is defined as:(71)

$$\chi_{ii} = \frac{\mu_0 \mu_B^2}{3k_B T} g_{ii}^2 \frac{\sum_{S_T} S_T (S_T + 1) (2S_T + 1) e^{-E_{(S_T)}/k_B T}}{\sum_{S_T} (2S_T + 1) e^{-E_{(S_T)}/k_B T}}, \quad (1.10)$$

where  $E_{(S_T)}$  is given by expressions in Table 1.5 for different symmetric conditions of a three-coupled spin system (Figure S2.10b) and  $S_T$  is same as defined before. Using equation 1.10, equation 1.9 can be rewritten as:

$$\begin{aligned} \delta_{PCS} &= 10^6 \frac{\mu_0 \mu_B^2}{4\pi 9k_B T r^3} \left\{ \left( g_{zz}^2 - \frac{1}{2} (g_{xx}^2 + g_{yy}^2) \right) (1 - 3\cos^2\theta) \right. \\ &\quad \left. + \left( \frac{3}{2} (g_{yy}^2 - g_{xx}^2) \sin^2\theta \cos 2\varphi \right) \right\} \frac{\sum_{S_T} S_T (S_T + 1) (2S_T + 1) e^{-E_{(S_T)}/k_B T}}{\sum_{S_T} (2S_T + 1) e^{-E_{(S_T)}/k_B T}} \end{aligned} \quad (1.11)$$

Using equation 1.11 one can estimate the PCS contribution to the observed chemical shift (equation 1.1). It can be used to refine the structure of the metalloproteins by providing distance restraints.(68)

## Paramagnetic NMR of laccase

The  $\text{Cu}^{2+}$  ions at the TNC exhibit a strong magnetic coupling that alleviates the problem of the line broadening observed in isolated type 1 copper proteins.(68) The two antiferromagnetically coupled coppers (Figure 1.3) at the T3 site of the RO state behave as a diamagnetic system at low temperatures (< 100 K), however, at elevated temperatures (> 100 K), low lying excited states are populated that are paramagnetic ( $S = 1$ ), resulting in paramagnetically shifted NMR resonances from the surrounding nuclei.(68, 78) The strong coupling between the coppers at the T3 site increases the electronic relaxation rate of the electron spins, reducing the paramagnetic broadening of nuclear resonances. The T2 site is not (strongly) coupled to the T3 coppers in the RO state, so the relaxation time of the electron spin is much longer, resulting in broadening beyond detection of resonances for nearby nuclear spins. In the NI state however, nuclei near to all the three coppers in the TNC are observed because the T3 and T2 sites are coupled via an oxygen atom (Figure 1.3), forming a frustrated spin system with a spin multiplicity of 2, which results in rapid electronic relaxation and relatively narrow lines for nuclear resonances. In this thesis a small laccase from *S. coelicolor* (SLAC) was used. To study the TNC, a mutant was employed in which the cysteine C288 coordinating the T1 copper ion (Figure 1.2a) was mutated to serine, depleting the T1 site of copper (SLAC-T1D). It was found that for this variant the NI state is dominant (Chapters 2 and 3), while for the wild type SLAC the RO state is most populated (Chapter 4).(73)

## Introduction

Paramagnetic ions decrease the spin lattice relaxation time ( $T_1$ ) of the nearby nuclei to a few milliseconds compared to the more distant nuclear spins, which have  $T_1$  times of hundreds of milliseconds. The water eliminated Fourier transform (WEFT) pulse sequence (Figure 1.5a) capitalizes on these differences of the  $T_1$  times to observe signals from nuclei close to the paramagnetic metal centre.(68, 79) Coupled with rapid pulsing with an inter-scan delay of a few ms, the WEFT pulse sequence can specifically detect the signals from nuclei experiencing the paramagnetic relaxation enhancement.(68) The temperature dependence of the  $^1\text{H}$  chemical shift from the NI state of SLAC-T1D was shown to consist of resonances having three different behaviours, Curie, anti-Curie and no-Curie.(73) This strongly suggests the presence of more than one coupling between the copper ions because for a single coupling a single temperature dependency is expected for all the resonances.(80, 81) Since in the NI state all the three copper ions at the TNC are coupled, three different couplings can be present (Figure 1.3). The coupling strengths  $J$  were reported to be  $-150\text{ cm}^{-1}$ ,  $-120\text{ cm}^{-1}$  and  $-80\text{ cm}^{-1}$ , (73) corresponding to the  $E_{(S_T)}$  values (expression from Table 1.5 for the general case where  $J_{13} \neq J_{12} \neq J_{23}$ ) of  $-235\text{ cm}^{-1}$ ,  $-114\text{ cm}^{-1}$  and  $175\text{ cm}^{-1}$  for the ground state, first excited doublet state and the second excited quartet state respectively. This results in a low-lying excited state at  $121\text{ cm}^{-1}$ , which is in close agreement with the variable temperature MCD measurement that placed this state at  $150\text{ cm}^{-1}$ .(73, 82) These observations suggest a triad configuration of the NI state with three copper ions coupled to each other with different strength.(73, 82) In contrast, for the wild type SLAC the temperature dependence of the  $^1\text{H}$  chemical shift shows a single Cu-Cu coupling consistent with the RO state.(73)

The above observations confirm the magnetic character of the NI and the RO states. To characterize underlying motions at the TNC multidimensional NMR experiments are needed. The 2D exchange spectroscopy (EXSY)(83) (Figure 1.5b) was reported to reveal chemical exchange process in the paramagnetic systems.(68, 84, 85) Nuclear Overhauser enhancements (NOE) can also be present in the EXSY spectrum because exchange and cross relaxation can both occur during the mixing time, in which magnetization is longitudinal. Chemical exchange can be distinguished from NOE signals by the temperature dependence of the volume integral of cross peaks. The volume of the NOE cross peak will not change much with increasing temperature, while it does increase for the exchange cross peak because the exchange rate is temperature dependent.(68) In this work, the EXSY/NOESY (Figure 1.5b) pulse sequence was used to identify chemical exchange processes and NOE cross peaks between protons at the TNC of SLAC (Chapters 2 and 3). 2D  $^{15}\text{N}$ - $^1\text{H}$  heteronuclear experiments can also be performed to determine the type of heteroatom a paramagnetically shifted  $^1\text{H}$  resonance is attached to.(68, 86) The evolution period in such experiments is optimized, based on the transverse relaxation time ( $T_2$ ) of the paramagnetically shifted proton resonances.(68) In this study the paramagnetically

# Introduction

tailored 2D  $^{15}\text{N}$ - $^1\text{H}$  heteronuclear multiple quantum coherence (HMQC) (Figure 1.5c) was used to correlate  $^{15}\text{N}$  and  $^1\text{H}$  nuclei via  $^1J$  coupling (Chapters 2 and 3).<sup>(87)</sup>

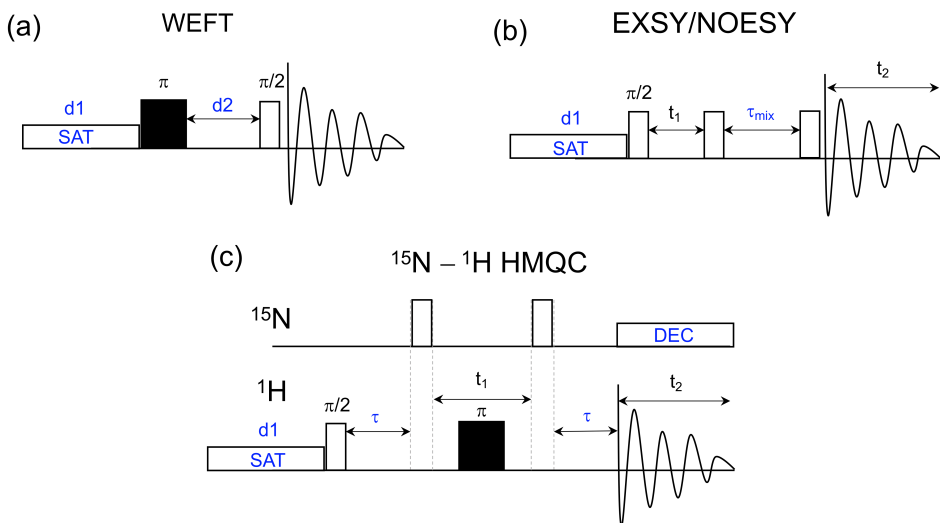


**Figure 1.5.** NMR pulse sequences to study the TNC of small laccase from *S. coelicolor*. (a) 1D water eliminated Fourier transfer (WEFT), where  $d2$  is the WEFT delay,<sup>(79)</sup> (b) 2D EXSY/NOESY where  $\tau_{\text{mix}}$  is the mixing time <sup>(83)</sup> and (c) 2D  $^{15}\text{N}$ - $^1\text{H}$  HMQC, where  $\tau$  is the magnetization transfer delay and DEC is the decoupling.<sup>(87)</sup> A continuous wave water saturation (SAT) is used during the interscan delay ( $d1$ ). The incremental delay or the evolution time  $t_1$  and the acquisition time  $t_2$  are shown in panels b and c. Open and filled rectangles represents  $\pi/2$  and  $\pi$  pulses, respectively.

## 1.4 Aim and Scope

Motional information about the TNC of SLAC is absent, yet it is expected that switching between conformations of the enzyme will be important in catalysing the successive steps of the four-electron reduction of molecular oxygen. The aim of the thesis is to lay the groundwork for detailed studies of the catalysis by laccase and the role of motions using NMR spectroscopy. Signals of nuclear spins very close to the site of oxygen reduction can be used as spies to report on structure and dynamics, provided the signals can be assigned to specific nuclei. A large part of the work presented in this thesis is focussed at that goal. In **Chapter 2** the presence of chemical exchange in the copper ligands in the TNC of the SLAC-T1D is reported. **Chapter 3** shows the first sequence specific assignment of the resonances to the T2 site histidine ligands by comparing SLAC-T1D and a double mutant SLAC-T1D/Y108F. In addition, the NMR

spectral regions of NI and RO states in SLAC-T1D are characterized in detail. In **Chapter 4** the NMR spectrum of SLAC-wt, its comparison with SLAC-T1D and assignment of T3 site histidine ligands using a double mutant SLAC-T1D/Q291E are reported. The role of the second shell residue Gln291 in stabilizing the RO state is demonstrated. **Chapter 5** discusses the results of quantum mechanical calculations on the RO state of the TNC. These calculations can be a step towards resonance assignment. Solid-state NMR (ssNMR) was shown to provide picometer resolution of the copper site in superoxide dismutase.(88) In addition, measuring the dipolar coupling strength of the nuclei near the copper center can provide us with motional information. Optimization and parameterization of suitable pulse sequences for application of ssNMR to laccase is important. This is shown in **Chapter 6** on a model copper compound. **Chapter 7** presents the general discussion and outlook.

## 1.5 References

1. Jeon, W.-Y., J.-H. Lee, K. Dashnyam, Y.-B. Choi, T.-H. Kim, H.-H. Lee, H.-W. Kim, and H.-H. Kim. 2019. Performance of a glucose-reactive enzyme-based biofuel cell system for biomedical applications. *Scientific Reports*. 9:1–9.
2. Mano, N., and A. de Poulpique. 2017. O<sub>2</sub> Reduction in Enzymatic Biofuel Cells. *Chem. Rev.*
3. Wang, J., K. Wang, F.-B. Wang, and X.-H. Xia. 2014. Bioinspired copper catalyst effective for both reduction and evolution of oxygen. *Nat Commun*. 5:5285.
4. Bullen, R.A., T.C. Arnot, J.B. Lakeman, and F.C. Walsh. 2006. Biofuel cells and their development. *Biosensors and Bioelectronics*. 21:2015–2045.
5. Southcott, M., K. MacVittie, J. Halánek, L. Halámková, W.D. Jemison, R. Lobel, and E. Katz. 2013. A pacemaker powered by an implantable biofuel cell operating under conditions mimicking the human blood circulatory system – battery not included. *Phys. Chem. Chem. Phys.* 15:6278.
6. Slaughter, G., and T. Kulkarni. 2019. Detection of Human Plasma Glucose Using a Self-Powered Glucose Biosensor. *Energies*. 12:825.
7. Vincent, K.A., J.A. Cracknell, J.R. Clark, M. Ludwig, O. Lenz, B. Friedrich, and F.A. Armstrong. 2006. Electricity from low-level H<sub>2</sub> in still air – an ultimate test for an oxygen tolerant hydrogenase. *Chem. Commun.* 5033.
8. Vincent, K.A., J.A. Cracknell, A. Parkin, and F.A. Armstrong. 2005. Hydrogen cycling by enzymes: electrocatalysis and implications for future energy technology. *Dalton Trans.* 3397.
9. Cinquin, P., C. Gondran, F. Giroud, S. Mazabrard, A. Pellissier, F. Boucher, J.-P. Alcaraz, K. Gorgy, F. Lenouvel, S. Mathé, P. Porcu, and S. Cosnier. 2010. A Glucose BioFuel Cell Implanted in Rats. *PLoS ONE*. 5:e10476.
10. Zebda, A., S. Cosnier, J.-P. Alcaraz, M. Holzinger, A. Le Goff, C. Gondran, F. Boucher, F. Giroud, K. Gorgy, H. Lamraoui, and P. Cinquin. 2013. Single Glucose Biofuel Cells Implanted in Rats Power Electronic Devices. *Scientific Reports*. 3:1–5.
11. Chen, X., L. Yin, J. Lv, A.J. Gross, M. Le, N.G. Gutierrez, Y. Li, I. Jeerapan, F. Giroud, A. Berezovska, R.K. O'Reilly, S. Xu, S. Cosnier, and J. Wang. 2019. Stretchable and Flexible Buckypaper-Based Lactate Biofuel Cell for Wearable Electronics. *Advanced Functional Materials*. 29:1905785.
12. Sony Develops. *Sony Global - Sony Global Headquarters*.
13. Flexer, V., and N. Mano. 2010. From Dynamic Measurements of Photosynthesis in a Living Plant to Sunlight Transformation into Electricity. *Anal. Chem.* 82:1444–1449.
14. Xiao, X., H. Xia, R. Wu, L. Bai, L. Yan, E. Magner, S. Cosnier, E. Lojou, Z. Zhu, and A. Liu. 2019. Tackling the Challenges of Enzymatic (Bio)Fuel Cells. *Chem. Rev.* 119:9509–9558.
15. Calabrese Barton, S., J. Gallaway, and P. Atanassov. 2004. Enzymatic Biofuel Cells for Implantable and Microscale Devices. *Chem. Rev.* 104:4867–4886.

16. Thiagarajan, N., D. Janmanchi, Y.-F. Tsai, W.H. Wana, R. Ramu, S.I. Chan, J.-M. Zen, and S.S.-F. Yu. 2018. A Carbon Electrode Functionalized by a Tricopper Cluster Complex: Overcoming Overpotential and Production of Hydrogen Peroxide in the Oxygen Reduction Reaction. *Angewandte Chemie International Edition*. 57:3612–3616.
17. Thorseth, M.A., C.E. Tornow, E.C.M. Tse, and A.A. Gewirth. 2013. Cu complexes that catalyze the oxygen reduction reaction. *Coordination Chemistry Reviews*. 257:130–139.
18. Gewirth, A.A., and M.S. Thorum. 2010. Electroreduction of Dioxygen for Fuel-Cell Applications: Materials and Challenges. *Inorg. Chem.* 49:3557–3566.
19. A Laccase-Wiring Redox Hydrogel for Efficient Catalysis of O<sub>2</sub> Electroreduction | The Journal of Physical Chemistry B. .
20. Kato, M., and I. Yagi. 2020. Electrocatalytic Oxygen Reduction at Multinuclear Metal Active Sites Inspired by Metalloenzymes. *e-J. Surf. Sci. Nanotechnol.* 18:81–93.
21. He, F., L. Mi, Y. Shen, X. Chen, Y. Yang, H. Mei, S. Liu, T. Mori, and Y. Zhang. 2017. Driving electrochemical oxygen reduction and hydrazine oxidation reaction by enzyme-inspired polymeric Cu(3,3'-diaminobenzidine) catalyst. *J. Mater. Chem. A*. 5:17413–17420.
22. Thorseth, M.A., C.S. Letko, E.C.M. Tse, T.B. Rauchfuss, and A.A. Gewirth. 2013. Ligand Effects on the Overpotential for Dioxygen Reduction by Tris(2-pyridylmethyl)amine Derivatives. *Inorg. Chem.* 52:628–634.
23. Tahsini, L., H. Kotani, Y.-M. Lee, J. Cho, W. Nam, K.D. Karlin, and S. Fukuzumi. 2012. Electron-Transfer Reduction of Dinuclear Copper Peroxo and Bis-μ-oxo Complexes Leading to the Catalytic Four-Electron Reduction of Dioxygen to Water. *Chemistry – A European Journal*. 18:1084–1093.
24. Fukuzumi, S., L. Tahsini, Y.-M. Lee, K. Ohkubo, W. Nam, and K.D. Karlin. 2012. Factors That Control Catalytic Two- versus Four-Electron Reduction of Dioxygen by Copper Complexes. *J. Am. Chem. Soc.* 134:7025–7035.
25. Solomon, E.I., D.E. Heppner, E.M. Johnston, J.W. Ginsbach, J. Cirera, M. Qayyum, M.T. Kieber-Emmons, C.H. Kjaergaard, R.G. Hadt, and L. Tian. 2014. Copper Active Sites in Biology. *Chemical Reviews*. 114:3659–3853.
26. Vallee, B.L., and R.J. Williams. 1968. Metalloenzymes: the entatic nature of their active sites. *Proc Natl Acad Sci U S A*. 59:498–505.
27. Dicke, B., A. Hoffmann, J. Stanek, M.S. Rampp, B. Grimm-Lebsanft, F. Biebl, D. Rukser, B. Maerz, D. Göries, M. Naumova, M. Biednov, G. Neuber, A. Wetzel, S.M. Hofmann, P. Roedig, A. Meents, J. Bielecki, J. Andreasson, K.R. Beyerlein, H.N. Chapman, C. Bressler, W. Zinth, M. Rübhausen, and S. Herres-Pawlis. 2018. Transferring the entatic-state principle to copper photochemistry. *Nature Chemistry*.
28. Williams, R.J.P. 1995. Energised (entatic) States of Groups and of Secondary Structures in Proteins and Metalloproteins. *European Journal of Biochemistry*. 234:363–381.
29. Jones, S.M., and E.I. Solomon. 2015. Electron Transfer and Reaction Mechanism of Laccases. *Cell Mol Life Sci.* 72:869–883.
30. Comba, P. 2000. Coordination compounds in the entatic state. *Coordination Chemistry Reviews*. 200–202:217–245.
31. Quintanar, L., C. Stoj, T.-P. Wang, D.J. Kosman, and E.I. Solomon. 2005. Role of Aspartate 94 in the Decay of the Peroxide Intermediate in the Multicopper Oxidase Fet3p. *Biochemistry*. 44:6081–6091.
32. Yoon, J., and E.I. Solomon. 2007. Electronic Structure of the Peroxy Intermediate and Its Correlation to the Native Intermediate in the Multicopper Oxidases: Insights into the Reductive Cleavage of the O–O Bond. *J. Am. Chem. Soc.* 129:13127–13136.
33. Augustine, A.J., C. Kjaergaard, M. Qayyum, L. Ziegler, D.J. Kosman, K.O. Hodgson, B. Hedman, and E.I. Solomon. 2010. Systematic Perturbation of the Trinuclear Copper Cluster in the Multicopper Oxidases: The Role of Active Site Asymmetry in Its Reduction of O<sub>2</sub> to H<sub>2</sub>O. *J. Am. Chem. Soc.* 132:6057–6067.
34. Carver, C.T., B.D. Matson, and J.M. Mayer. 2012. Electrocatalytic Oxygen Reduction by Iron Tetra-arylporphyrins Bearing Pendant Proton Relays. *J. Am. Chem. Soc.* 134:5444–5447.
35. Plapp, B.V. 2010. Conformational Changes and Catalysis by Alcohol Dehydrogenase. *Arch Biochem Biophys*. 493:3–12.



36. Henzler-Wildman, K.A., V. Thai, M. Lei, M. Ott, M. Wolf-Watz, T. Fenn, E. Pozharski, M.A. Wilson, G.A. Petsko, M. Karplus, C.G. Hübner, and D. Kern. 2007. Intrinsic motions along an enzymatic reaction trajectory. *Nature*. 450:838–844.
37. Serrano-Posada, H., S. Centeno-Leija, S.P. Rojas-Trejo, C. Rodríguez-Almazán, V. Stojanoff, and E. Rudiño-Piñera. 2015. X-ray-induced catalytic active-site reduction of a multicopper oxidase: structural insights into the proton-relay mechanism and O<sub>2</sub>-reduction states. *Acta Cryst D*. 71:2396–2411.
38. Silva, C.S., P. Durão, A. Fillat, P.F. Lindley, L.O. Martins, and I. Bento. 2012. Crystal structure of the multicopper oxidase from the pathogenic bacterium *Campylobacter jejuni* CGUG11284: characterization of a metallo-oxidase. *Metallomics*. 4:37–47.
39. Machczynski, M.C., E. Vijgenboom, B. Samyn, and G.W. Canters. 2004. Characterization of SLAC: A small laccase from *Streptomyces coelicolor* with unprecedented activity. *Protein Science*. 13:2388–2397.
40. Sherif, M., D. Waung, B. Korbeci, V. Mavisakalyan, R. Flick, G. Brown, M. Abou-Zaid, A.F. Yakunin, and E.R. Master. 2013. Biochemical studies of the multicopper oxidase (small laccase) from *Streptomyces coelicolor* using bioactive phytochemicals and site-directed mutagenesis. *Microb Biotechnol*. 6:588–597.
41. Lörcher, S., P. Lopes, A. Kartashov, and E.E. Ferapontova. 2013. Direct Bio-electrocatalysis of O<sub>2</sub> Reduction by *Streptomyces coelicolor* Laccase Orientated at Promoter-Modified Graphite Electrodes. *ChemPhysChem*. 14:2112–2124.
42. Gallaway, J., I. Wheeldon, R. Rincon, P. Atanassov, S. Banta, and S.C. Barton. 2008. Oxygen-reducing enzyme cathodes produced from SLAC, a small laccase from *Streptomyces coelicolor*. *Biosensors and Bioelectronics*. 23:1229–1235.
43. Langerman, M., and D.G.H. Hetterscheid. 2019. Fast Oxygen Reduction Catalyzed by a Copper(II) Tris(2-pyridylmethyl)amine Complex through a Stepwise Mechanism. *Angewandte Chemie*. 131:13108–13112.
44. Liu, C., H. Lei, Z. Zhang, F. Chen, and R. Cao. 2017. Oxygen reduction catalyzed by a water-soluble binuclear copper(II) complex from a neutral aqueous solution. *Chem. Commun*. 53:3189–3192.
45. Kato, M., K. Kimijima, M. Shibata, H. Notsu, K. Ogino, K. Inokuma, N. Ohta, H. Uehara, Y. Uemura, N. Oyaizu, T. Ohba, S. Takakusagi, K. Asakura, and I. Yagi. 2015. Deprotonation of a dinuclear copper complex of 3,5-diamino-1,2,4-triazole for high oxygen reduction activity. *Physical Chemistry Chemical Physics*. 17:8638–8641.
46. Janusz, G., A. Pawlik, U. Świdarska-Burek, J. Polak, J. Sulej, A. Jarosz-Wilkolazka, and A. Paszczyński. 2020. Laccase Properties, Physiological Functions, and Evolution. *International Journal of Molecular Sciences*. 21:966.
47. Sekretaryova, A., S.M. Jones, and E.I. Solomon. 2019. O<sub>2</sub> Reduction to Water by High Potential Multicopper Oxidases: Contributions of the T1 Copper Site Potential and the Local Environment of the Trinuclear Copper Cluster. *J. Am. Chem. Soc*. 141:11304–11314.
48. Toscano, M.D., L.D. Maria, S. Lobedanz, and L.H. Østergaard. 2013. Optimization of a Small Laccase by Active-Site Redesign. *ChemBioChem*. 14:1209–1211.
49. Mate, D.M., and M. Alcalde. 2015. Laccase engineering: From rational design to directed evolution. *Biotechnology Advances*. 33:25–40.
50. Gunne, M., A. Höppner, P.-L. Hagedoorn, and V.B. Urlacher. 2014. Structural and redox properties of the small laccase Ssl1 from *Streptomyces svaceus*. *The FEBS Journal*. 281:4307–4318.
51. Mate, D.M., D. Gonzalez-Perez, M. Falk, R. Kittl, M. Pita, A.L. De Lacey, R. Ludwig, S. Shleev, and M. Alcalde. 2013. Blood Tolerant Laccase by Directed Evolution. *Chemistry & Biology*. 20:223–231.
52. Scheiblbrandner, S., E. Breslmayr, F. Csarman, R. Paukner, J. Führer, P.L. Herzog, S.V. Shleev, E.M. Osipov, T.V. Tikhonova, V.O. Popov, D. Haltrich, R. Ludwig, and R. Kittl. 2017. Evolving stability and pH-dependent activity of the high redox potential *Botrytis aclada* laccase for enzymatic fuel cells. *Sci Rep*. 7:13688.
53. Olbrich, A.C., J.N. Schild, and V.B. Urlacher. 2019. Correlation between the T1 copper reduction potential and catalytic activity of a small laccase. *Journal of Inorganic Biochemistry*. 201:110843.

54. Gabdulkhakov, A.G., O.S. Kostareva, I.A. Kolyadenko, A.O. Mikhaylina, L.I. Trubitsina, and S.V. Tishchenko. 2018. Incorporation of Copper Ions into T2/T3 Centers of Two-Domain Laccases. *Molecular Biology*. 52:23–29.
55. Gabdulkhakov, A., I. Kolyadenko, O. Kostareva, A. Mikhaylina, P. Oliveira, P. Tamagnini, A. Lisov, and S. Tishchenko. 2019. Investigations of Accessibility of T2/T3 Copper Center of Two-Domain Laccase from *Streptomyces griseoflavus* Ac-993. *International Journal of Molecular Sciences*. 20:3184.
56. Trubitsina, L.I., S.V. Tishchenko, A.G. Gabdulkhakov, A.V. Lisov, M.V. Zakharova, and A.A. Leontievsky. 2015. Structural and functional characterization of two-domain laccase from *Streptomyces viridochromogenes*. *Biochimie*. 112:151–159.
57. Palmer, A.E., S.K. Lee, and E.I. Solomon. 2001. Decay of the Peroxide Intermediate in Laccase: Reductive Cleavage of the O–O Bond. *J. Am. Chem. Soc.* 123:6591–6599.
58. Gupta, A., I. Nederlof, S. Sottini, A.W.J.W. Tepper, E.J.J. Groenen, E.A.J. Thomassen, and G.W. Canters. 2012. Involvement of Tyr108 in the Enzyme Mechanism of the Small Laccase from *Streptomyces coelicolor*. *Journal of the American Chemical Society*. 134:18213–18216.
59. Kielb, P., H.B. Gray, and J.R. Winkler. 2020. Does Tyrosine Protect *S. Coelicolor* Laccase from Oxidative Degradation? DOI: 10.26434/chemrxiv.12671612.v1
60. Tepper, A.W.J.W., S. Milikisyants, S. Sottini, E. Vijgenboom, E.J.J. Groenen, and G.W. Canters. 2009. Identification of a Radical Intermediate in the Enzymatic Reduction of Oxygen by a Small Laccase. *J. Am. Chem. Soc.* 131:11680–11682.
61. Skálová, T., J. Dohnálek, L.H. Østergaard, P.R. Østergaard, P. Kolenko, J. Dušková, A. Štěpánková, and J. Hašek. 2009. The Structure of the Small Laccase from *Streptomyces coelicolor* Reveals a Link between Laccases and Nitrite Reductases. *Journal of Molecular Biology*. 385:1165–1178.
62. Matera, I., A. Gullotto, S. Tilli, M. Ferraroni, A. Scozzafava, and F. Briganti. 2008. Crystal structure of the blue multicopper oxidase from the white-rot fungus *Trametes trogii* complexed with p-toluate. *Inorganica Chimica Acta*. 361:4129–4137.
63. Enguita, F.J., L.O. Martins, A.O. Henriques, and M.A. Carrondo. 2003. Crystal Structure of a bacterial endospore coat component a laccase with enhanced thermostability properties. *J. Biol. Chem.* 278:19416–19425.
64. Augustine, A.J., L. Quintanar, C.S. Stoj, D.J. Kosman, and E.I. Solomon. 2007. Spectroscopic and Kinetic Studies of Perturbed Trinuclear Copper Clusters: The Role of Protons in Reductive Cleavage of the O–O Bond in the Multicopper Oxidase Fet3p. *J. Am. Chem. Soc.* 129:13118–13126.
65. Heppner, D.E., C.H. Kjaergaard, and E.I. Solomon. 2014. Mechanism of the Reduction of the Native Intermediate in the Multicopper Oxidases: Insights into Rapid Intramolecular Electron Transfer in Turnover. *J. Am. Chem. Soc.* 136:17788–17801.
66. Tian, S., S.M. Jones, and E.I. Solomon. 2020. Role of a Tyrosine Radical in Human Ceruloplasmin Catalysis. *ACS Cent. Sci.*
67. Quintanar, L., J. Yoon, C.P. Aznar, A.E. Palmer, K.K. Andersson, R.D. Britt, and E.I. Solomon. 2005. Spectroscopic and Electronic Structure Studies of the Trinuclear Cu Cluster Active Site of the Multicopper Oxidase Laccase: Nature of Its Coordination Unsaturation. *J. Am. Chem. Soc.* 127:13832–13845.
68. Bertini, I., C. Luchinat, G. Parigi, and E. Ravera. 2017. NMR of paramagnetic molecules: applications to metalloproteins and models. Second edition. Amsterdam: Elsevier.
69. Kambe, K. 1950. On the Paramagnetic Susceptibilities of Some Polynuclear Complex Salts. *J. Phys. Soc. Jpn.* 5:48–51.
70. Gruber, S.J., C.M. Harris, and E. Sinn. 1968. Metal Complexes as Ligands. VI. Antiferromagnetic Interactions in Trinuclear Complexes Containing Similar and Dissimilar Metals. *The Journal of Chemical Physics*. 49:2183–2191.
71. Sinn, E. 1970. Magnetic exchange in polynuclear metal complexes. *Coordination Chemistry Reviews*. 5:313–347.
72. Lee, S.-K., S.D. George, W.E. Antholine, B. Hedman, K.O. Hodgson, and E.I. Solomon. 2002. Nature of the Intermediate Formed in the Reduction of O<sub>2</sub> to H<sub>2</sub>O at the Trinuclear Copper Cluster Active Site in Native Laccase. *J. Am. Chem. Soc.* 124:6180–6193.

73. Machczynski, M.C., and J.T. Babicz. 2016. Correlating the structures and activities of the resting oxidized and native intermediate states of a small laccase by paramagnetic NMR. *Journal of Inorganic Biochemistry*. 159:62–69.
74. Griffith, J.S. 1972. On the general theory of magnetic susceptibilities of polynuclear transition-metal compounds. In: *Structure and Bonding*. Berlin, Heidelberg: Springer Berlin Heidelberg. pp. 87–126.
75. M. Ubbink, J. A. R. Worrall, G. W. Canters, E. J. J. Groenen, and M. Huber. 2002. Paramagnetic Resonance of Biological Metal Centers. *Annual Review of Biophysics and Biomolecular Structure*. 31:393–422.
76. Kurland, R.J., and B.R. McGarvey. 1970. Isotropic NMR shifts in transition metal complexes: The calculation of the fermi contact and pseudocontact terms. *Journal of Magnetic Resonance (1969)*. 2:286–301.
77. McConnell, H.M., and R.E. Robertson. 1958. Isotropic Nuclear Resonance Shifts. *The Journal of Chemical Physics*. 29:1361–1365.
78. Bertini, I., C. Luchinat, and G. Parigi. 2002. Magnetic susceptibility in paramagnetic NMR. *Progress in Nuclear Magnetic Resonance Spectroscopy*. 40:249–273.
79. Patt, S.L., and B.D. Sykes. 1972. Water Eliminated Fourier Transform NMR Spectroscopy. *J. Chem. Phys.* 56:3182–3184.
80. Banci, L., I. Bertini, and C. Luchinat. 1990. The  $^1\text{H}$  NMR parameters of magnetically coupled dimers—The Fe<sub>2</sub>S<sub>2</sub> proteins as an example. In: *Bioinorganic Chemistry*. Berlin, Heidelberg: Springer. pp. 113–136.
81. Asokan, A., B. Varghese, and P.T. Manoharan. 1999. Synthesis, Structure, Magnetic Properties, and  $^1\text{H}$  NMR Studies of a Moderately Antiferromagnetically Coupled Binuclear Copper(II) Complex. *Inorganic Chemistry*. 38:4393–4399.
82. Solomon, E.I., A.J. Augustine, and J. Yoon. 2008. O<sub>2</sub> Reduction to H<sub>2</sub>O by the multicopper oxidases. *Dalton Trans.* 3921–3932.
83. Jeener, J., B.H. Meier, P. Bachmann, and R.R. Ernst. 1979. Investigation of exchange processes by two-dimensional NMR spectroscopy. *J. Chem. Phys.* 71:4546–4553.
84. Santos, H., D.L. Turner, A.V. Xavier, and J. le Gall. 1984. Two-dimensional NMR studies of electron transfer in cytochrome c<sub>3</sub>. *Journal of Magnetic Resonance (1969)*. 59:177–180.
85. Bertini, I., C. Luchinat, G. Parigi, and R. Pierattelli. 2005. NMR Spectroscopy of Paramagnetic Metalloproteins. *ChemBioChem*. 6:1536–1549.
86. Ciofi-Baffoni, S., A. Gallo, R. Muzzioli, and M. Piccioli. 2014. The IR- $^{15}\text{N}$ -HSQC-AP experiment: a new tool for NMR spectroscopy of paramagnetic molecules. *Journal of Biomolecular NMR*. 58:123–128.
87. Bax, A., R.H. Griffey, and B.L. Hawkins. 1983. Correlation of proton and nitrogen-15 chemical shifts by multiple quantum NMR. *Journal of Magnetic Resonance (1969)*. 55:301–315.
88. Bertarello, A., L. Benda, K.J. Sanders, A.J. Pell, M.J. Knight, V. Pelmeshnikov, L. Gonnelli, I.C. Felli, M. Kaupp, L. Emsley, R. Pierattelli, and G. Pintacuda. 2020. Picometer Resolution Structure of the Coordination Sphere in the Metal-Binding Site in a Metalloprotein by NMR. *J. Am. Chem. Soc.* 142:16757–16765.

